



# Numerical Heat Transfer, Part A: Applications

An International Journal of Computation and Methodology

ISSN: (Print) (Online) Journal homepage: <https://www.tandfonline.com/loi/unht20>

## Two-dimensional pore-scale investigation of liquid water evolution in the cathode of proton exchange membrane fuel cells

Wen-Zhen Fang , Jin Li & Wen-Quan Tao

To cite this article: Wen-Zhen Fang , Jin Li & Wen-Quan Tao (2020): Two-dimensional pore-scale investigation of liquid water evolution in the cathode of proton exchange membrane fuel cells, Numerical Heat Transfer, Part A: Applications, DOI: [10.1080/10407782.2020.1845558](https://doi.org/10.1080/10407782.2020.1845558)

To link to this article: <https://doi.org/10.1080/10407782.2020.1845558>



Published online: 13 Nov 2020.



Submit your article to this journal [↗](#)



View related articles [↗](#)



View Crossmark data [↗](#)



# Two-dimensional pore-scale investigation of liquid water evolution in the cathode of proton exchange membrane fuel cells

Wen-Zhen Fang<sup>a</sup>, Jin Li<sup>b</sup>, and Wen-Quan Tao<sup>a</sup>

<sup>a</sup>Key Laboratory of Thermo-Fluid Science and Engineering, Ministry of Education, Xi'an Jiaotong University, Shaanxi, P.R. China; <sup>b</sup>Zhengzhou Yutong Group Co., Ltd., Henan, P.R. China

## ABSTRACT

Water management is crucial to the performance of proton exchange membrane fuel cells (PEMFC). In this work, a pore-scale model is developed based on lattice Boltzmann (LB) method for the simulation of multi-component multiphase reactive transport in an operating PEMFC, with the aim to capture the water vapor generation, condensation, and subsequent transport in the entire porous cathode, including the catalyst layer, gas diffusion layer, and gas channel. The current LB model considers the effect of liquid/vapor condensation on the dynamic evolution of liquid water. The transportation of oxygen and dynamic water evolution is coupled by the electrochemical reactions occurring at the active site of the catalyst layer. Effects of the microstructure and wettability of gas diffusion layer, vapor generation rate, temperature distribution, and existence of the rib on the dynamic evolution of liquid water are elaborated. The insights provided in this work would facilitate the understanding of liquid water evolution in the PEMFC and reduce its water flooding issues.

## ARTICLE HISTORY

Received 24 September 2020  
Accepted 30 October 2020

## 1. Introduction

The proton exchange membrane fuel cell (PEMFC) is a promising power source for various applications due to its advantages in high power density, high energy efficiency, and low emissions. To achieve the high performance of PEMFC, the water management in the PEMFC, particularly in the cathode side, is of great importance [1–3]. Specifically, a certain humidity is necessary to maintain the conductivity of the proton in membrane, or otherwise, the dehydration of membrane would reduce the cell performance due to the great ohmic loss across the membrane. On the other hand, water flooding issues would occur if the catalyst layer (CL), gas diffusion layer (GDL), or gas channel (GC) in the PEMFC are filled with liquid water, which hinders the transport of reactant gases and reduces the reactive surface, limiting the maximum achievable current density. To tackle this issue, lots of experimental studies [4–7] and numerical simulations [8–11] have been conducted to investigate the water management in the PEMFC. However, most of them focused on the drainage process of liquid water within the hydrophobic GDL, in which the non-wetting liquid water displacing the gas is dominated by the capillary pressure. Although many visualization experiments [5–7] have been conducted to observe the dynamic transport of liquid water in the PEMFC, direct observation is still difficult to fully understand water evolution mechanisms in the complicated structure of GDL. By now, two typical liquid water transport

mechanisms in the GDL have been proposed. One is the branching-type geometry of liquid water distribution model proposed by Nam and Kaviany [12] with the aid of environmental scanning electron microscopy (ESEM), through which the following processes can be observed: water vapor condenses on the surfaces of micro-droplets which then agglomerate to be large macro-droplets, and finally merge to form a continuous liquid water cluster flow. Another water transport mechanism is the fingering and channeling model proposed by Lister et al. [13] through an *ex-situ* visualization experiment of liquid water transport in the GDL, in which the liquid water preferentially intrudes into pores with the largest diameter and finally permeates through the GDL. However, those models may not work for the transport of liquid water in a practically operating PEMFC. In this regard, Hartnig et al. [6, 7] observed the water transport in an operating PEMFC by the synchrotron X-ray radiography with a high spatial resolution of  $3\ \mu\text{m}$ . The *in-situ* visualization experiments have demonstrated that the vapor condensation plays a crucial role in the water transport in the PEMFC. Thus, the capillary pressure and vapor condensation should be considered as two major factors contributing to the water evolution in an operating PEMFC.

Understanding the water transport mechanism in PEMFC by experiments alone is difficult, and numerical models can help. In this regard, Basu et al. [14] adopted the multiphase mixture model to reveal the effects of phase change on the water evolution inside the cathode of the PEMFC, which needs empirical relations to close the model. Straubhaar et al. [15, 16] adopted the pore network method to simulate the water vapor condensation within the GDL on the cathode side. Nowadays, the lattice Boltzmann method (LBM) has been developed as a powerful technique to simulate the multiphase flow and mass transport processes, and it is particularly successful in applications involving complex geometries [17–20]. Chen et al. [17] adopted multiphase LBM to investigate liquid water transport in GDL and GC, and found that liquid water transport process is capillary fingering. Zhou and Wu [21] adopted the Shan–Chen multiphase lattice Boltzmann (LB) model to simulate the water vapor condensation in the GDL, in which a nonphysical source term is added at the GDL/CL boundary to represent the water vapor diffusing into the GDL from CL. Molaeimanesh and Akbari [22, 23] developed a LB model to simulate the single-phase, multi-species reactive flow in the cathode of PEMFC, but they neglected the effect of liquid–vapor phase change.

As shown above, most of the existing simulations focused on the water transport in the GDL without the detailed information in the adjacent CL. At the GDL/CL boundary, they usually assumed all the entry water (from CL to GDL) to be the liquid phase or vapor phase [15, 16]. In this work, we propose a new pore-scale model based on LB to investigate of multicomponent multiphase reactive transport process in the entire cathode of PEMFC, including the CL, GDL, and GC. In the CL, the oxygen consumption and water vapor generation at active sites are considered. The water state at the GDL/CL interface depends on the local condensation situation. Besides, the present LB model can deal with a large liquid/vapor density ratio, which is close to the real ratio at the operating temperature of  $80\ ^\circ\text{C}$ . To the authors' knowledge, it is the first pore-scale study to investigate the vapor generation, condensation, and subsequent water transportation in the entire cathode of PEMFC with liquid/vapor density ratio close to reality.

The simulation process of the present article is described as follows. The oxygen transports from GC to GDL and finally diffuses into CL, and then the oxygen is consumed while the water vapor is gradually generated at the reactive site in the CL. Once the concentration of water vapor exceeds the local saturation level, vapor condenses into liquid water and then transports in the cathode of PEMFC. In general, it is a multicomponent multiphase reactive problem and the existing multicomponent multiphase Shan–Chen models can be adopted to solve those issues. However, the existing multicomponent multiphase Shan–Chen model is restricted to the small density ratio of liquid and gas [24, 25]. Therefore, we adopted a modified single-component multiphase model to simulate water vapor condensation with a large liquid/vapor density ratio ( $\sim 2,000$ ), by neglecting the effect of oxygen on the dynamic transport of water. The

transportation of oxygen and dynamic evolution of water vapor are coupled by the electrochemical reactions occurring at the active site of the CL. Although the water vapor condensation is affected by the temperature distribution in the cathode, a given temperature distribution is assigned in the computational domain instead of solving the energy governing equation for the convenience of numerical simulation without loss of major physical characteristics.

The rest of this article is organized as follows. The numerical models are introduced in Section 2. Then, the accuracy of the present model is validated in Section 3. The influences of wettability of GDL, reaction coefficient, temperature distribution, and existence of the rib in GC on the transport of liquid water are discussed in Section 4. Finally, several conclusions are drawn in Section 5.

## 2. Numerical method

### 2.1. MRT pseudopotential lattice Boltzmann method

We consider a D2Q9 LB model with a multiple-relaxation-time collision operator

$$f_i(\mathbf{x} + \mathbf{c}_i \delta t, t + \delta t) - f_i(\mathbf{x}, t) = -(\mathbf{M}^{-1} \mathbf{S} \mathbf{M})_{ij} [f_j - f_j^{eq}] + \delta t F'_i \quad (1)$$

where  $\mathbf{x}$  denotes the position,  $\delta t$  is the time step,  $f_i$  is the density distribution function, and  $f_i^{eq}$  is the equilibrium distribution function, given by

$$f_i^{eq} = \omega_i \rho \left[ 1 + \frac{\mathbf{c}_i \cdot \mathbf{u}}{c_s^2} + \frac{(\mathbf{c}_i \cdot \mathbf{u})^2}{2c_s^4} - \frac{\mathbf{u}^2}{2c_s^2} \right] \quad (2)$$

where  $\omega_0 = 4/9$ ,  $\omega_{1-4} = 1/9$ ,  $\omega_{5-8} = 1/36$ . In Eq. (1),  $\mathbf{M}$  is an orthogonal transformation matrix

$$\mathbf{M} = \begin{bmatrix} 1, & 1, & 1, & 1, & 1, & 1, & 1, & 1, & 1 \\ -4, & -1, & -1, & -1, & -1, & 2, & 2, & 2, & 2 \\ 4, & -2, & -2, & -2, & -2, & 1, & 1, & 1, & 1 \\ 0, & 1, & 0, & -1, & 0, & 1, & -1, & -1, & 1 \\ 0, & -2, & 0, & 2, & 0, & 1, & -1, & -1, & 1 \\ 0, & 0, & 1, & 0, & -1, & 1, & 1, & -1, & -1 \\ 0, & 0, & -2, & 0, & 2, & 1, & 1, & -1, & -1 \\ 0, & 1, & -1, & 1, & -1, & 0, & 0, & 0, & 0 \\ 0, & 0, & 0, & 0, & 0, & 1, & -1, & 1, & -1 \end{bmatrix} \quad (3)$$

and  $\mathbf{S}$  is a diagonal matrix

$$\mathbf{S} = \text{diag}(\tau_\rho^{-1}, \tau_e^{-1}, \tau_\zeta^{-1}, \tau_j^{-1}, \tau_q^{-1}, \tau_j^{-1}, \tau_q^{-1}, \tau_v^{-1}, \tau_v^{-1}) \quad (4)$$

in which  $\tau_\nu$  is the relaxation time coefficient related to the kinematic viscosity

$$\tau_\nu = \frac{\nu}{c_s^2 \delta t} + 0.5 \quad (5)$$

In Eq. (1),  $F'_i$  is the force term, calculated by

$$\mathbf{F}' = \mathbf{M}^{-1} \left( \mathbf{I} - \frac{1}{2} \mathbf{S} \right) \mathbf{M} \bar{\mathbf{F}} \quad (6)$$

where  $\mathbf{F}' = (F'_0, F'_1, \dots, F'_8)^T$ ,  $\mathbf{I}$  is the identity matrix, and  $\bar{\mathbf{F}} = (\bar{F}_0, \bar{F}_1, \dots, \bar{F}_8)^T$  with

$$\bar{F}_i = \omega_i \left[ \frac{\mathbf{c}_i \cdot \mathbf{F}}{c_s^2} + \frac{\mathbf{uF} : (\mathbf{c}_i \mathbf{c}_i - c_s^2 \mathbf{I})}{2c_s^4} \right] \quad (7)$$

The macroscopic density and velocity can be obtained by

$$\rho = \sum_i f_i \quad (8)$$

$$\rho \mathbf{u} = \sum_i \mathbf{c}_i f_i + \frac{\delta t}{2} \mathbf{F} \quad (9)$$

where  $\mathbf{F} = (F_x, F_y)$  is the total force acting on the fluid particle, including the fluid–fluid interaction force  $\mathbf{F}_f$ , fluid–solid interaction force  $\mathbf{F}_s$ , and body force  $\mathbf{F}_b$ . In this work, an improved force scheme is adopted to improve the thermodynamic consistency [18, 26]

$$\mathbf{F}_m = \mathbf{M} \bar{\mathbf{F}} = \begin{bmatrix} 0 \\ 6\mathbf{uF} + \frac{12\sigma |\mathbf{F}_f|^2}{\psi^2 \delta_t (\tau_e - 0.5)} \\ -6\mathbf{uF} - \frac{12\sigma |\mathbf{F}_f|^2}{\psi^2 \delta_t (\tau_\zeta - 0.5)} \\ F_x \\ -F_x \\ F_y \\ -F_y \\ 2(uF_x - vF_y) \\ (uF_y + vF_x) \end{bmatrix} \quad (10)$$

where  $\sigma$  is a parameter that can be used to tune the mechanical stability condition, which can be determined by a preliminary numerical test of a suspended circular droplet. In Eq. (10),  $|\mathbf{F}_f|^2 = (F_{f,x}^2 + F_{f,y}^2)$ , in which  $\mathbf{F}_f$  is the fluid–fluid interaction force

$$\mathbf{F}_f = -G\psi(\mathbf{x}) \sum_i w(|\mathbf{c}_i|^2) \psi(\mathbf{x} + \mathbf{c}_i) \mathbf{c}_i \quad (11)$$

where  $G$  is the interaction strength and  $\psi$  is the pseudopotential, defined as

$$\psi(\mathbf{x}) = \sqrt{2(p_{\text{EOS}} - \rho c_s^2)/Gc^2} \quad (12)$$

where  $p_{\text{EOS}}$  is the non-ideal equation of state. In this work, the Peng–Robinson (P-R) equation of state is adopted [27]

$$p_{\text{EOS}} = \frac{\rho RT}{1 - b\rho} - \frac{a\varphi(T)\rho^2}{1 + 2b\rho - b^2\rho^2} \quad (13)$$

$$\varphi(T) = \left[ 1 + (0.37464 + 1.54226\omega - 0.26992\omega^2) \left( 1 - \sqrt{T/T_c} \right) \right]^2$$

where  $a = 0.45724R^2T_c^2/p_c$  and  $b = 0.0778RT_c/p_c$ . The fluid–solid interaction force can be calculated by

$$\mathbf{F}_s = -G_w\psi(\mathbf{x}) \sum_i w(|\mathbf{e}_i|^2) \psi(\mathbf{x}) S(\mathbf{x} + \mathbf{e}_i) \mathbf{e}_i \quad (14)$$

where  $S$  is the indicator function which equals 1 for solids and 0 for fluids, and  $G_w$  is used to tune the wettability of the surface.

## 2.2. Mass transport LB model

For the mass transport in the cathode of PEMFC, the evolution equation of distribution function can be expressed as [11, 28]

$$g_i(\mathbf{x} + \mathbf{e}_i \delta_t, t + \delta_t) - g_i(\mathbf{x}, t) = -\frac{1}{\tau_D} [g_i - g_i^{eq}] \quad (15)$$

where the equivalent distribution function  $g_i^{eq}$  is defined as

$$g_i^{eq} = \omega_i C \quad (16)$$

where  $C$  represents the concentration. For the mass transport problem, the D2Q9 LB model can be reduced to D2Q5 model without the loss of accuracy. In Eq. (16),  $\omega_i$  is given by

$$\omega_i = \begin{cases} \omega_0 \\ (1 - \omega_0)/4 \end{cases} \quad (17)$$

where the fraction  $\omega_0$  can be selected from 0 to 1. The concentration can be obtained by

$$C = \sum_i g_i \quad (18)$$

The macroscopic diffusivity is related to the relaxation time coefficient

$$D = \frac{1}{2}(1 - \omega_0)(\tau_D - 0.5) \quad (19)$$

## 2.3. Computational domain and boundary conditions

The computational domain is the entire cathode in the PEMFC, which includes the GC, GDL, and CL, as schematically shown in Figure 1. The thicknesses of the CL, GDL, and GC are set to be 40  $\mu\text{m}$ , 160  $\mu\text{m}$ , and 136  $\mu\text{m}$ , respectively. The thickness of the GC is shortened to save the computational resource. The computational domain is discretized into  $600 \times 840$  grids, and each grid represents 0.4  $\mu\text{m}$ . The solid surfaces in the CL domain are the reactive sites where the electrochemical reaction takes place. If the solid surfaces in the CL domain are covered by liquid water, they become inactive.

The periodic boundary conditions are applied at the  $x$ -direction. For the fluid flow, the top and bottom sides of the computational domain are assigned to be wall conditions to trap all the generated water vapor. While for the oxygen diffusion, a constant concentration is applied on the top side. At the interface of fluid–solid boundaries at the GDL region, the bounce back treatments are adopted to achieve the no slip or no flux conditions. Due to the low solubility of oxygen in the liquid water, the liquid water is assumed to be insoluble to the oxygen.

As for the reactive boundaries at the CL region where electrochemical reactions take place, the modified bounce back treatment is adopted to consider the additional vapor flux due to the reaction. If the fluid–solid interface is put at the midway between two nodes (as shown in Figure 2a), the modified bounce back conditions yield [29–31]

$$g_i = \bar{g}_i + \Delta\phi_g \quad (20)$$

$$f_i = \bar{f}_i + \frac{2\omega_i}{c_s^2} \Delta\phi_f \quad (21)$$

where the subscript  $i$  represents the direction leaving from walls while  $\bar{i}$  toward walls.  $\Delta\phi_g$  and  $\Delta\phi_f$  are the diffusive and advective flux due to the reaction for mass transport and fluid flow LB models, respectively, and can be obtained by [32, 33]

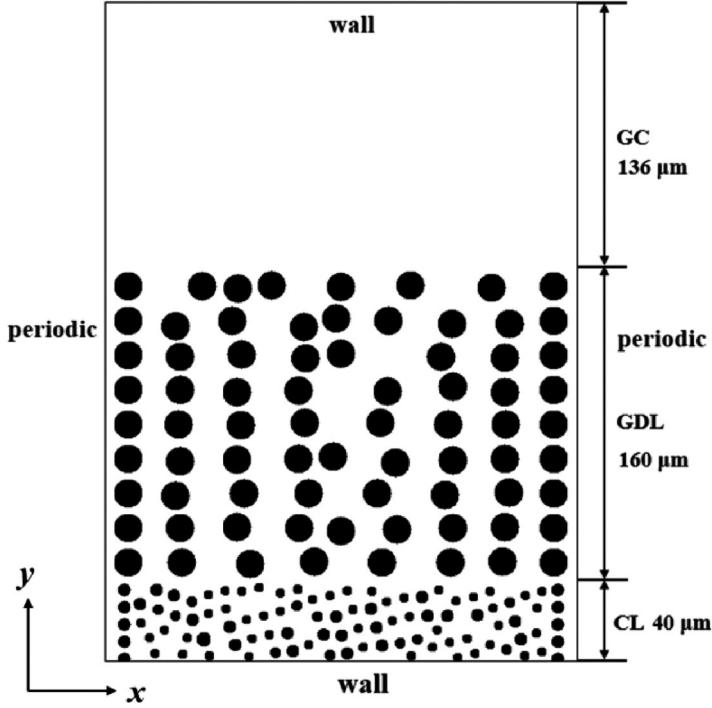


**Figure 1.** The reconstructed microstructure of the cathode in PEMFC, including the CL, GDL, and GC.

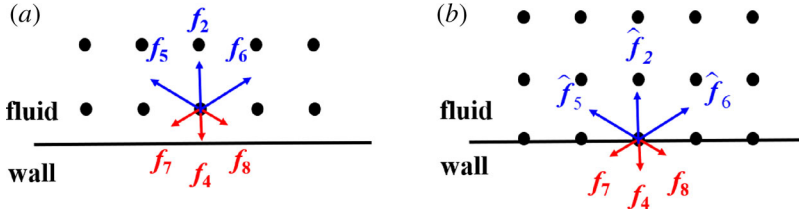


**Figure 2.** The schemes for the reactive boundaries at fluid–solid interfaces. (a) Interface located at the midway between two nodes; (b) interface located at the reaction surface.

$$\Delta\phi_g = \frac{\tau_D}{\tau_D - 0.5} D \frac{\partial C}{\partial x} = -\frac{\tau_D}{\tau_D - 0.5} k C_{O_2} \quad (22)$$

$$\Delta\phi_f = \rho v = k C_{O_2} \times M_{H_2O} \quad (23)$$

where  $k$  is the reaction coefficient which can be obtained from the Butler–Volmer equation [34]

$$k = \frac{A_s}{4F} \frac{I^{\text{ref}}}{C_{O_2}^{\text{ref}}} \left\{ \exp\left(\frac{\alpha F \eta}{RT}\right) - \exp\left(-\frac{(1-\alpha) F \eta}{RT}\right) \right\} \quad (24)$$

where  $A_s$  is the roughness factor,  $F$  is Faraday's constant,  $I^{\text{ref}}$ ,  $C^{\text{ref}}$  are the reference current density and oxygen concentration, respectively,  $\alpha$  is the transfer coefficient,  $\eta$  is the overpotential, and  $T$  is the temperature.

If the lattice node is put right on the reactive surface (as shown in Figure 2b), the modified bounce back conditions yield

$$\hat{g}_i = g_i + \Delta\phi'_g \quad (25)$$

$$\hat{f}_i = f_i + \frac{2\omega_i}{c_s^2} \Delta\phi_f \quad (26)$$

where  $\hat{g}$  and  $\hat{f}$  denote distribution functions before streaming, and

$$\Delta\phi'_g = -kC_{O_2} \quad (27)$$

The oxygen concentration on the reactive surface is unknown. According to Kang et al. [35, 36], the following expression can be used to calculate the concentration at the reactive surface

$$C_{O_2} = \frac{2g_i}{k + 2\omega_i} \quad (28)$$

It should be noted that the difference in the calculation of the diffusive flux between Eq. (22) and Eq. (27) results from the truncation errors at the internal nodes and boundary nodes [35]. Their effectiveness and accuracy will be validated in Section 3.2. The local properties of Eqs. (25)–(27) make them easier to implement parallel computing, and thus we adopted the treatment of Eqs. (25)–(27) to deal with the surface reactive boundary condition.

### 3. Validation

#### 3.1. The pseudopotential multiphase LB model

As indicated above, the modified pseudopotential multiphase LB model is adopted to simulate the two-phase flow in the cathode of the PEMFC. As reported in Ref. [18, 26], a smaller value of  $a$  in the P-R equation of state improves the numerical stability. Thus, we choose  $a = 2/490$ . Besides,  $\sigma = 0.118$  (in Eq. (10)) is determined after a series preliminary test of the two-dimensional suspension droplet. With the determined parameters, the comparison of the coexistence curve of liquid drop and gas between numerical results and Maxwell solutions [37] are shown in Figure 3a, which shows good agreement. In this case, the reduced temperature can be as low as  $0.5 T_c$ , and the liquid–vapor density ratio can be over 10,000.

The fluid–solid interaction force can be tuned by the parameter  $G_w$  in Eq. (14) to control the wettability of the wall. The variation of contact angle *versus*  $G_w$  is shown in Figure 3b. The surface is hydrophilic for  $G_w < 0$  with contact angle lower than  $90^\circ$  while hydrophobic for  $G_w > 0$ .

#### 3.2. Surface reactive boundaries

Considering a one-dimensional diffusion problem in a channel with the reactive surface at the boundary ( $x = l$ ), the governing equations are

$$\begin{aligned} \frac{\partial C}{\partial t} &= D \frac{\partial^2 C}{\partial x^2} \\ C(x, t = 0) &= 1 \\ \frac{\partial C}{\partial x} \Big|_{x=0} &= 0; D \frac{\partial C}{\partial x} \Big|_{x=l} = -kC \end{aligned} \quad (29)$$

It has the analytical solution

$$C(x, t) = \sum_{n=1}^{\infty} \frac{4 \sin(\lambda_n)}{2\lambda_n + \sin(2\lambda_n)} e^{-\lambda_n^2 Fo} \cos\left(\lambda_n \frac{x}{l}\right) \quad (30)$$

where

$$\lambda_n \tan(\lambda_n) = Da, Da = \frac{kl}{D}, Fo = \frac{Dt}{l^2} \quad (31)$$

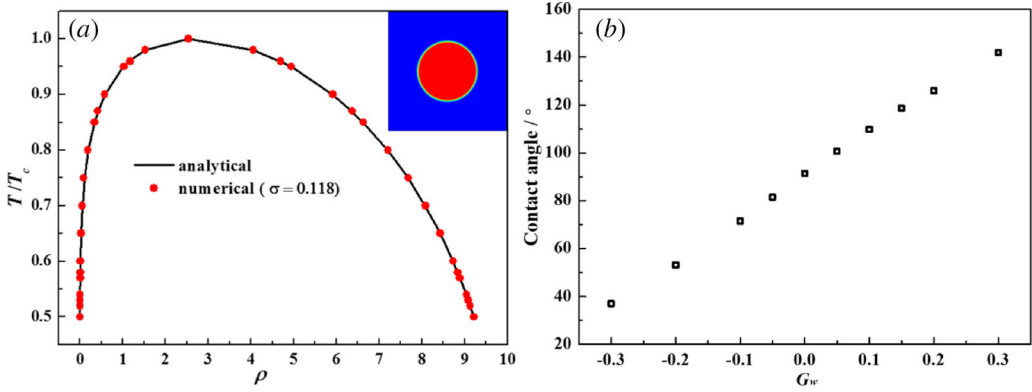


Figure 3. Validation of pseudopotential LB model: (a) coexistence curve; (b) contact angle versus  $G_w$ .

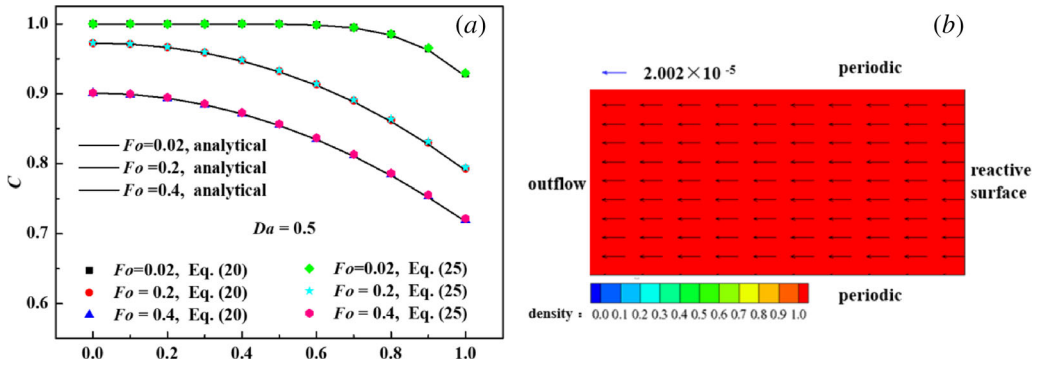


Figure 4. Validation of surface reactive boundary conditions: (a) mass transport LB model; (b) fluid flow LB model.

As discussed in Section 2.3, for the mass transport LB model, the surface reactive boundaries can be dealt with using Eq. (20) or Eq. (25). Figure 4a shows the comparison of the concentration profiles between numerical results and analytical solutions. It can be seen that the numerical results with Eq. (20) and Eq. (25) agree well with the analytical solutions, which validates the accuracy of the present model.

In the previous studies, most of the reactive flows use the passive approach in which one species is considered as a solvent while others are considered as solutes. The velocity field is solved for the solvent species, while other species are followed by the solutions of advection–diffusion equations based on the assumption that their consumption or generation does not affect the momentum of velocity field. However, in this work, when the electrochemical reaction occurs, the water vapor is continuously generated, which significantly increases the momentum of water vapor. To check the effectiveness of treatment of the surface reactive boundaries (Eq. (21) or Eq. (26)) to capture the net advective flux, a single-phase fluid flow in a channel with a reactive boundary is simulated, as shown in Figure 4b, in which the reactive surface can generate a net advective flux  $\rho u = -2 \times 10^{-5}$  (the minus sign indicating the flux direction toward negative  $x$ -direction). When the flow reaches the steady state, the magnitude of the velocity is  $2.002 \times 10^{-5}$  ( $\rho = 1$  in the entire domain), which confirms the effectiveness of the present model.

#### 4. Results and discussion

The simulation process is as follows: oxygen from GC diffuses into GDL and meets the CL where a reaction rate is specified. As the water vapor generates at the reactive sites in the CL during the

operation of PEMFC, the local concentration of water vapor increases and then diffuses into the GDL and GC. If the concentration of water vapor exceeds the local saturation level, the water vapor will condense.

In the following, the effect of cathode microstructure, temperature distribution, wettability of GDL and rib of GC on the water vapor generation, condensation, and subsequent transport in the entire porous cathode are presented.

#### 4.1. Cathodes with regular microstructures

The water vapor condensation in the PEMFC is affected by many factors, including the wettability of GDL, temperature gradient, vapor generation/transport rate, and microstructure. In this work, two microstructures have been studied, one is regular and the other is random. We first investigate the water evolution in a well-designed cathode with the regular microstructure. Figure 5 shows the water vapor generation, condensation, and subsequent transportation processes in the cathode with a mixed-wettability (coexistence of hydrophilic and hydrophobic) GDL. In the images, the black solids at the GDL domain are hydrophobic fibers with a static contact angle of  $110^\circ$  while the black solids covered by white surfaces denote hydrophilic fibers with a static contact angle of  $70^\circ$ . The wettability of solid particles in the CL is assumed to be neutral. The porosity of the GDL and CL in Figure 5a, b are 0.645 and 0.737, respectively, while the porosity of the GDL in Figure 5c is 0.802. A prescribed linear temperature distribution is assigned in the entire domain with the highest temperature of  $0.56 T_c$  at the CL side and the lowest temperature of  $0.545 T_c$  at the GC side.

From Figure 5a, b, we can find that the liquid water first appears in the CL domain, and then water vapor condenses at the small pores surrounded by the hydrophilic fibers near the GDL/CL interface. Subsequently, the water vapor condenses at the initial condensation positions in the GDL and grows up to penetrate the neighbor pores. The liquid water preferentially penetrates the hydrophilic pores other than hydrophobic pores due to the difference in the capillary pressure. By contrast, the water vapor is not condensed at the hydrophobic sites in the GDL and liquid water can not intrude into the hydrophobic GDL even when the CL is full of the liquid water due to the high capillary resistance.

In Figure 5c, hydrophilic fibers and hydrophobic fibers are spatially separated from each other. It can be seen that the hydrophilic site in the GDL near the GDL/GC interface is the initial condensation position. With the generation of water vapor, the liquid water continues to condense inside the GDL. Then, the liquid water in the GDL are aggregated to a water cluster. Besides, the liquid water in the CL is wicked from CL into GDL. Finally, the liquid droplet at the top of the GDL intrudes into the GC. By the comparison of results among three different spatial mixed-wettability of GDLs, we can find that the configuration of spatial mixed-wettability of GDL has a great influence on the liquid water transport in the cathode, and a proper configuration (e.g., Figure 5c) facilitates the removal of liquid water out of GDL.

At the GDL, the phenomenon that the water vapor first condenses at the small pores surrounded by the hydrophilic fibers can be explained by Kelvin's equation

$$RT \ln \frac{p}{p_0} = \frac{2\gamma M}{r\rho} \quad (32)$$

where  $p$  is the vapor pressure on the curved surface,  $p_0$  is the saturated vapor pressure when the surface is flat,  $\gamma$  is the surface tension, and  $r$  is the curvature radius (positive for convex curvature and negative for concave curvature). Kelvin's equation reveals that the saturated vapor pressure at hydrophilic pores is lower than that at hydrophobic pores, and also reveals that the saturated vapor pressure at the small pores is lower than that at large pores for the hydrophilic surface

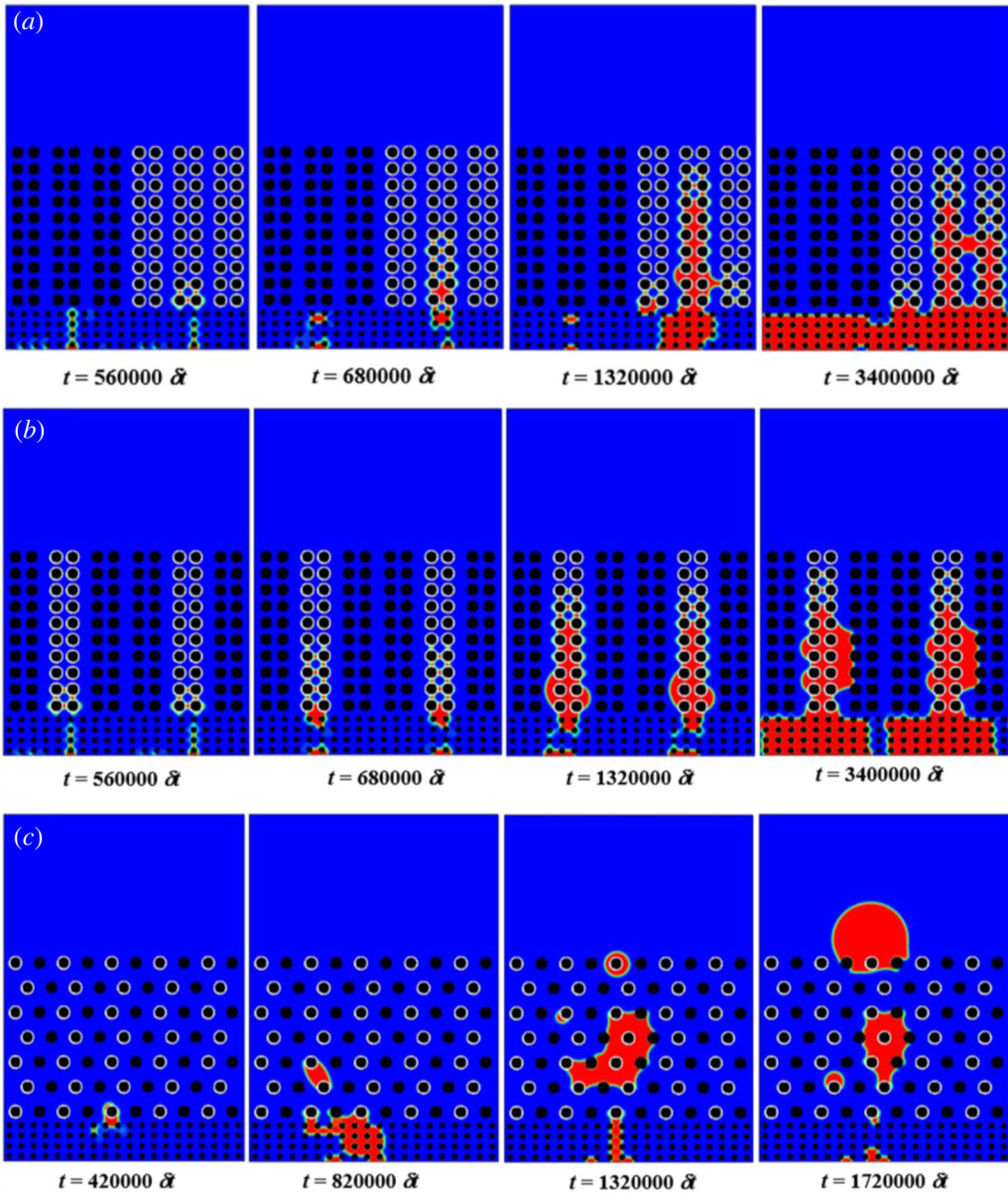


**Figure 5.** Dynamic evolutions of liquid water in cathodes with different spatial mixed-wettability of GDL: (a) Structure I, (b) Structure II, and (c) Structure III. The black solids in the GDL are hydrophobic while black solids covered with white surfaces are hydrophilic.

(concave curvature). The above results mean that the vapor is easier condensed at the hydrophilic small pores.

## 4.2. Cathodes with random microstructures

### 4.2.1. Effect of reaction rate

In the above discussion, both GDL and CL were assumed structured regularly. Generally speaking, the GDL and CL in the cathode are random porous media. In the following, the cathodes with random microstructures of the GDL and CL are investigated. The GDL is assumed to be

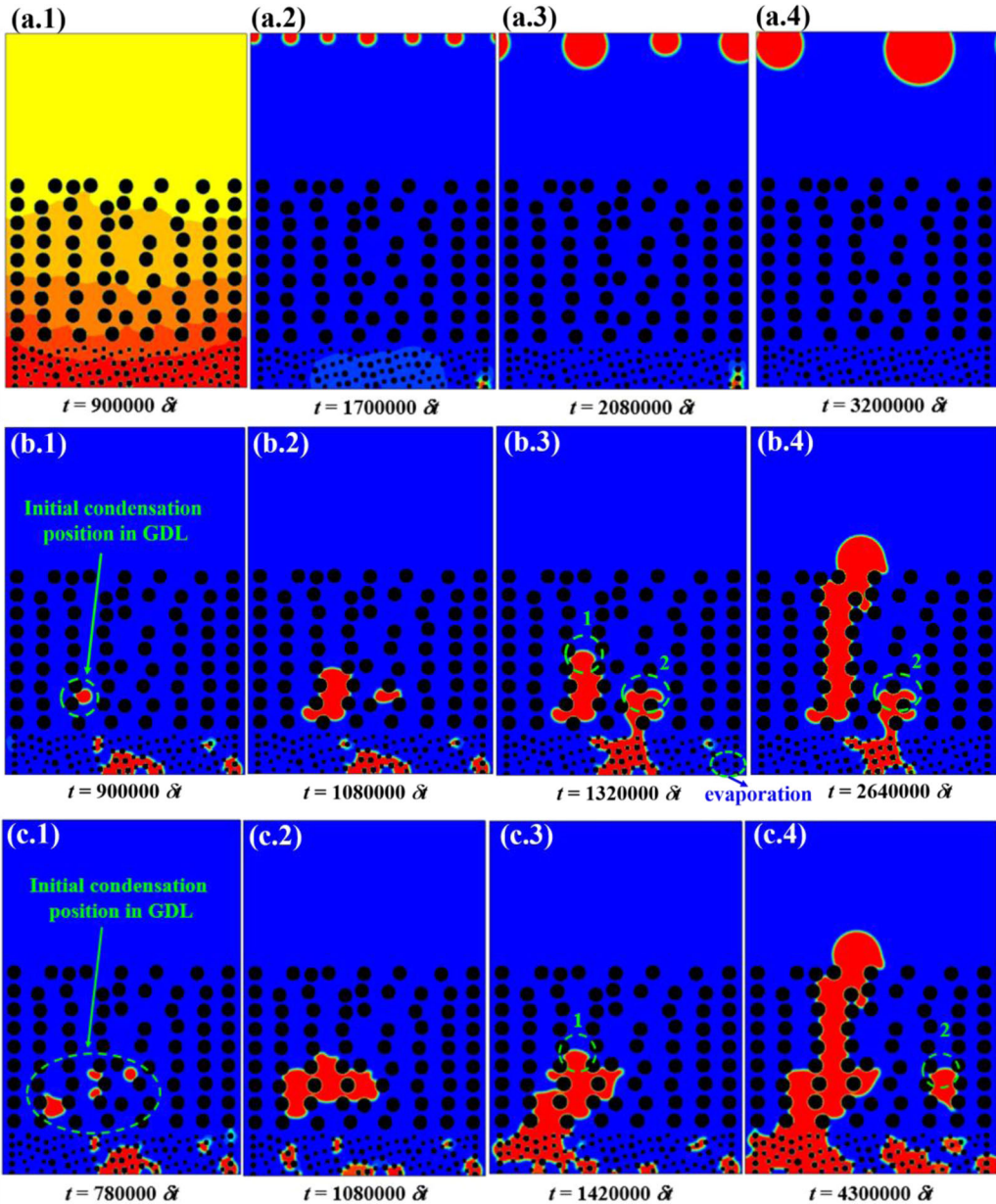
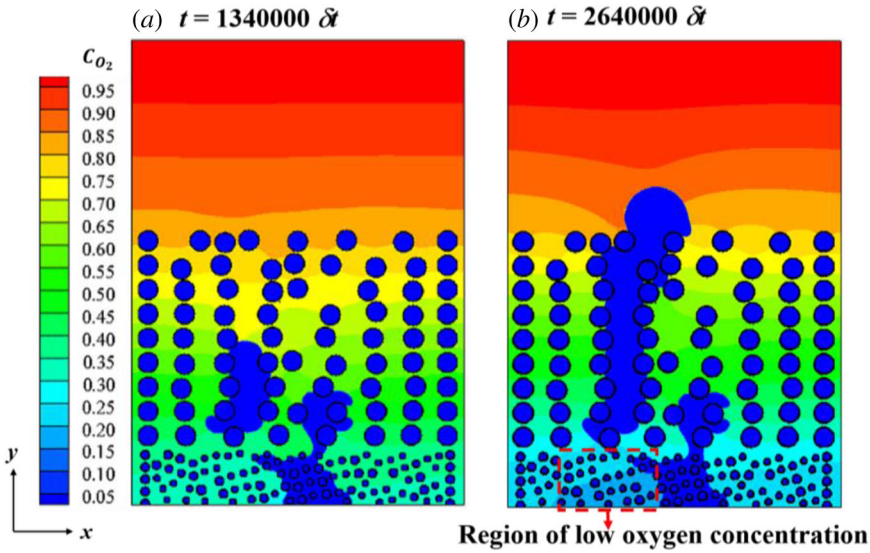


Figure 6. Dynamic evolutions of liquid water in the cathode at different overpotentials (a)  $\eta = 0.28$ , (b)  $\eta = 0.32$ , and (c)  $\eta = 0.34$ .

hydrophobic with a static contact angle of  $120^\circ$  while the CL is assumed to be neutral with a static contact angle of  $90^\circ$ . Likewise, a linear temperature distribution is assigned in the entire domain with the highest temperature of  $0.56 T_c$  at the CL side and the lowest temperature of  $0.545 T_c$  at the GC side. In the PEMFC, the overpotential is related to the current density, and a larger overpotential represents a higher electrochemical reaction rate on the reactive surfaces in the CL, which means an intensified generation rate of water vapor. At different overpotentials, the dynamic evolution of liquid water in the cathode with a random microstructure of GDL and CL is shown in Figure 6. As shown in Figure 6a, at a lower water vapor generation rate (with a small value of overpotential  $\eta = 0.28$ ), the generated water vapor has enough time to transport from CL into the GDL and GC, and the water vapor tends to condense at the top of GC due to



**Figure 7.** Oxygen concentration distributions in the cathode when  $\eta = 0.32$  is at different moments: (a)  $t = 13,400,00 \delta t$  and (b)  $t = 26,400,00 \delta t$ . Initially, the oxygen concentration is set to be unity. The upper concentration boundary is constant and set to be unity.

its lowest local temperature. As  $\eta$  increases, the water vapor accumulates in the CL since the water vapor transport rate is lower than the generation rate, resulting in the condensation of water vapor in the CL, as shown in Figure 6b, c.

From Figure 6b, c, it can be seen that initial condensation positions in the GDL significantly affect the water evolution in the cathode. The initial condensation positions serve as the embryo, and the water vapor continues to condense on the surface of initial droplet embryo. Then, the droplets grow up and are accumulated to form a large liquid water cluster. The liquid water in the GDL prefers to intrude into larger pores due to their smaller capillary resistance. Meanwhile, according to Kelvin's equation, the saturated water vapor pressure on a large droplet is lower than that on a small droplet for the hydrophobic surface (convex curvature), resulting in an easier condensation of water vapor on the front of large droplets. As the result, the water vapor continues to condense on the front of water cluster 1 (denoted in Figure 6b3, 6c3) which preferentially intrudes into the large pores until penetrates through the GDL, while water cluster 2 (denoted in Figure 6b4, 6c4) remains almost unchanged.

Figure 7 shows the corresponding oxygen concentration distributions in the cathode when  $\eta = 0.32$ . Initially, the concentration distribution of oxygen is set to be unity in the entire domain. It can be seen that the concentration of oxygen in the cathode decreases with time due to its consumption in the CL. Besides, the liquid water in the GDL hinders the mass transportation of oxygen from GC to CL (see the region of low oxygen concentration at CL in Figure 7b). Meanwhile, because of the low solubility of oxygen in the liquid water, solid particles in the CL covered by the liquid water no longer produce electrochemical reactions. Thus, the condensed liquid water in the cathode will greatly reduce the performance of PEMFC.

The variations of the water saturation degree at the CL, GDL, and GC domains at different overpotentials are shown in Figure 8. Here, the definition of water saturation degree at the porous media is the ratio of liquid water volume to void volume. At  $\eta = 0.34$ , the liquid water first emerges in the CL region, which later leads to a severe water flooding issue in the CL. In general, the water saturation increases with time at CL, GDL, and GC, but occasionally the decrease of water saturation could happen. It is mainly because the rapid condensation at one spot affects the quasi-steady liquid/vapor interface at other spot, further leading to the evaporation and redistribution of water. Note that the re-evaporation of already condensed liquid water can be seen in Figure 6b.

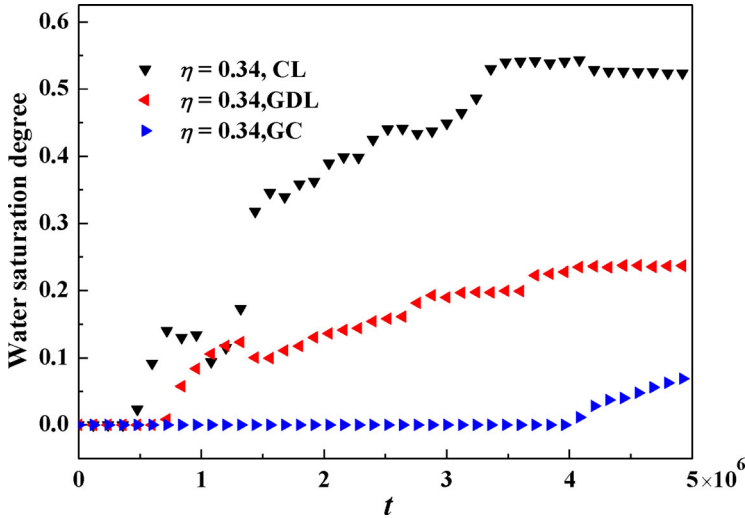


Figure 8. Variation of water saturation at CL, GDL, and GC domains versus time.

#### 4.2.2. Effect of temperature distribution

In the above studies, a prescribed linear temperature distribution is assigned to the entire domain which is decreasing from CL to GC. To study the effects of temperature distribution on the water evolution in the PEMFC, a uniform temperature distribution with  $T = 0.55 T_c$  is assigned to the entire domain while other conditions remain unchanged compared with the case of Figure 6b, and the results are provided in Figure 9. As shown in the figure, with a uniform temperature distribution, the generated water vapor tends to condense in the CL domain. The liquid water can not penetrate through GDL into GC and the water flooding issue in the CL becomes severe. Thus, the temperature distribution in the cathode has a significant effect on the dynamic evolution of liquid water. A lower temperature near the GC can facilitate the condensation of water vapor near the GC and reduce the water flooding issue in the CL.

#### 4.2.3. Effect of wettability of GDL

In Section 4.2.1, the GDL is assumed to be hydrophobic with a static contact angle of  $120^\circ$ . To study the effect of the wettability of GDL on dynamic evolution of liquid water, a hydrophilic GDL with a static contact angle of  $70^\circ$  is studied while other conditions remain unchanged compared with the case of Figure 6b. Figure 10 shows the dynamic evolution of water in a cathode with the hydrophilic GDL. Clearly, the water vapor tends to condense at small pore sizes in the hydrophilic GDL. Then, the growing liquid water fills in the small pores and is accumulated to occupy the large pores. Finally, the liquid water tends to occupy the entire GDL, which certainly significantly hinders the transportation of oxygen from GC to CL and further reduces the performance of PEMFC. Hence, it can be concluded that for the hydrophilic GDL, the liquid water in the GDL cannot intrude into the GC because the liquid water prefers to adhere on hydrophilic fibers in the GDL.

### 4.3. Gas channel with rib

For the flow field plate in the PEMFC, the rib and GC are coexisted. Due to the high thermal conductivity of the rib, the heat can be easily dissipated through the rib, resulting in a lower temperature at the region under the rib than others. Thus, in this study, a relatively low temperature is assigned at the region under the rib. Figure 11 shows the dynamic evolution of liquid water in a cathode with a rib in the GC. Here, the GDL is assumed to be hydrophobic with a static contact angle of  $120^\circ$ , while the wettability of rib is assumed to be slightly hydrophilic with a contact angle of  $80^\circ$ . As shown in Figure 11a,

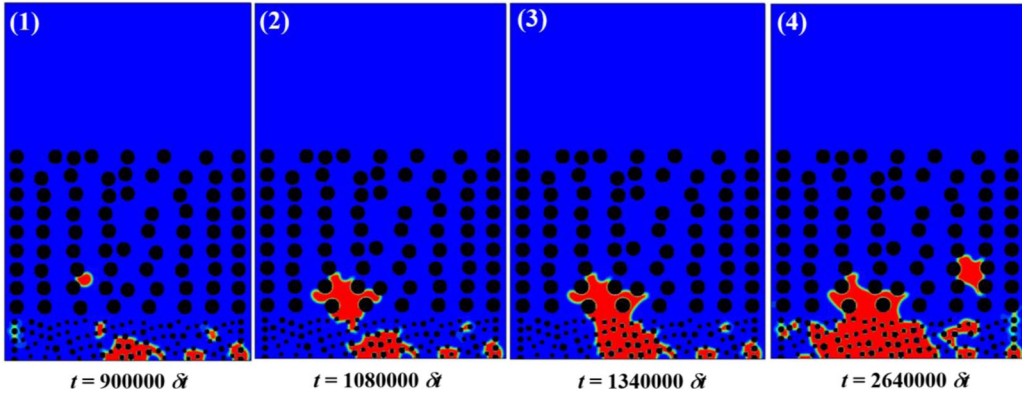


Figure 9. Dynamic evolution of liquid water in the cathode with a uniform temperature distribution when  $\eta = 0.32$ .

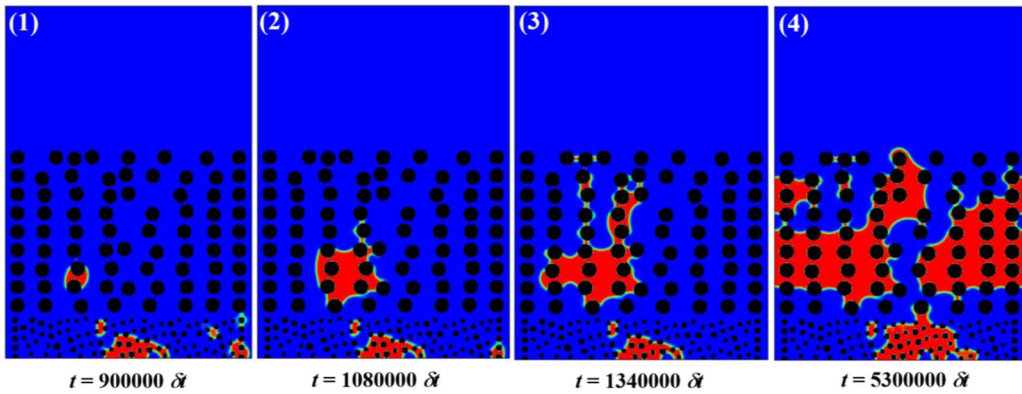


Figure 10. Dynamic evolution of liquid water in a cathode with hydrophilic GDL when  $\eta = 0.32$ .

at a low overpotential ( $\eta = 0.30$ ), the liquid water in the GDL first emerges in the region under the rib. Due to the low generation rate of water vapor, it has enough time to transport from CL into GDL and GC, and then condenses in the region under the rib with a lower temperature. The existence of the rib in the GC facilitates the condensation of water vapor in the region under the rib. Finally, the liquid water under the rib gradually grows up and preferentially intrudes into the GC. This phenomenon is similar to the *in-situ* visualization of water evolution in an operating fuel cell with a high-resolution synchrotron X-ray radiography conducted by Manke et al. [5].

In contrast, at a larger vapor generation rate when  $\eta = 0.32$ , the liquid water in the GDL first emerges at the region close to the CL, as shown in Figure 11b. With the condensation of water vapor, the liquid in the GDL grows up to be a water cluster. Subsequently, another water cluster emerges at the region under the rib. Finally, the water clusters are merged and intrude into the GC.

## 5. Conclusions

In this work, a pore-scale model based on the LBM is proposed to simulate the multicomponent multiphase reactive transport process in a cathode of the PEMFC. The proposed model is adopted to study the water vapor generation, condensation, and subsequent transport in the entire porous cathode of the PEMFC, including the CL, GDL, and GC. The following conclusions can be drawn.

1. The water vapor prefers to condense at the small hydrophilic pores near the GDL/CL interface. The configurations in the spatial mixed-wettability of GDLs affect the liquid water transport in the cathode, and a proper configuration of GDL can facilitate the removal of liquid water.

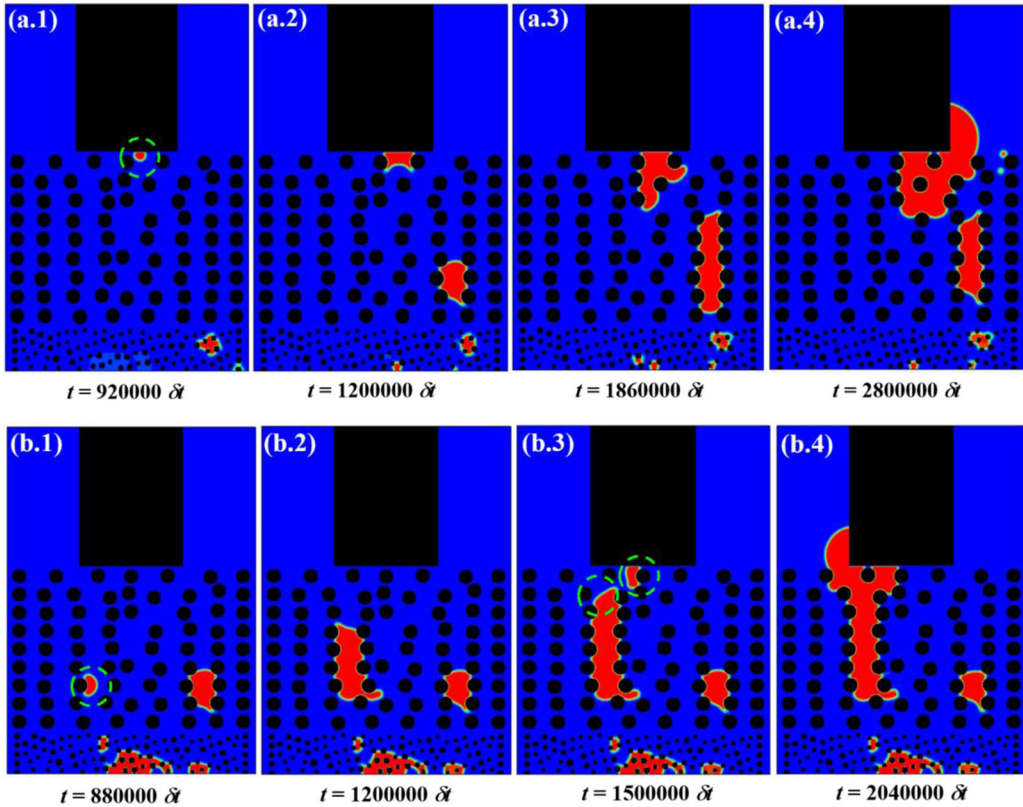


Figure 11. Dynamic evolution of liquid water in cathode with a land in GC: (a)  $\eta = 0.30$ ; (b)  $\eta = 0.32$ .

2. Condensation plays an important role in the liquid water evolution. The water vapor tends to condense on the surface of initial condensation embryos, and then penetrates into a preferential path with the lower capillary pressure and saturated vapor pressure.
3. The vapor generation rate affects the condensation sites at the cathode, and vapor prefers to condense on the GC at a low generation rate while tends to condense in the CL at a high generation rate. A lower temperature on the GC side can reduce the water flooding issue in the CL while a hydrophilic GDL would aggravate the water flooding.
4. The existence of the rib in the GC facilitates the condensation of water vapor in the region under the rib.

## Funding

This research was supported by the Key Project of National Natural Science Foundation of China (51836005), the National Key Research and Development Program of China (2017YFC0702700), the Key Science and Technology Project in Henan Province (Innovation Leading Project: 191110210200), and the Basic Research Project of Shaanxi Province (2019ZDXM3-01).

## References

- [1] A. Z. Weber and J. Newman, "Coupled thermal and water management in polymer electrolyte fuel cells," *J. Electrochem. Soc.*, vol. 153, no. 12, pp. A2205, 2006.
- [2] J. Zhao and X. Li, "A review of polymer electrolyte membrane fuel cell durability for vehicular applications: degradation modes and experimental techniques," *Energy Convers. Manage.*, vol. 199, pp. 112022, 2019. DOI: 10.1016/j.enconman.2019.112022.

- [3] J. Shen, Z. Tu, and S. H. Chan, "Enhancement of mass transfer in a proton exchange membrane fuel cell with blockage in the flow channel," *Appl. Therm. Eng.*, vol. 149, pp. 1408–1418, 2019.
- [4] K. Tüber, D. Pócza, and C. Hebling, "Visualization of water buildup in the cathode of a transparent PEM fuel cell," *J. Power Sources*, vol. 124, no. 2, pp. 403–414, 2003.
- [5] I. Manke, et al., "Investigation of water evolution and transport in fuel cells with high resolution synchrotron x-ray radiography," *Appl. Phys. Lett.*, vol. 90, no. 17, pp. 174105, 2007. DOI: [10.1063/1.2731440](https://doi.org/10.1063/1.2731440).
- [6] C. Hartnig, I. Manke, R. Kuhn, N. Kardjilov, J. Banhart, and W. Lehnert, "Cross-sectional insight in the water evolution and transport in polymer electrolyte fuel cells," *Appl. Phys. Lett.*, vol. 92, no. 13, pp. 134106, 2008. DOI: [10.1063/1.2907485](https://doi.org/10.1063/1.2907485).
- [7] C. Hartnig, I. Manke, R. Kuhn, S. Kleinau, J. R. Goebbels, and J. Banhart, "High-resolution in-plane investigation of the water evolution and transport in PEM fuel cells," *J. Power Sources*, vol. 188, no. 2, pp. 468–474, 2009.
- [8] B. Chen, Y. Cai, J. Shen, Z. Tu, and S. H. Chan, "Performance degradation of a proton exchange membrane fuel cell with dead-ended cathode and anode," *Appl. Therm. Eng.*, vol. 132, pp. 80–86, 2018.
- [9] P. K. Sinha, P. P. Mukherjee, and C.-Y. Wang, "Impact of GDL structure and wettability on water management in polymer electrolyte fuel cells," *J. Mater. Chem.*, vol. 17, no. 30, pp. 3089–3103, 2007.
- [10] P. P. Mukherjee, Q. Kang, and C.-Y. Wang, "Pore-scale modeling of two-phase transport in polymer electrolyte fuel cells-progress and perspective," *Energy Environ. Sci.*, vol. 4, no. 2, pp. 346–369, 2011.
- [11] G. Zhang and K. Jiao, "Multi-phase models for water and thermal management of proton exchange membrane fuel cell: a review," *J. Power Sources*, vol. 391, pp. 120–133, 2018.
- [12] J. H. Nam and M. Kaviany, "Effective diffusivity and water-saturation distribution in single-and two-layer PEMFC diffusion medium," *Int. J. Heat Mass Transfer*, vol. 46, no. 24, pp. 4595–4611, 2003.
- [13] S. Litster, D. Sinton, and N. Djilali, "Ex situ visualization of liquid water transport in PEM fuel cell gas diffusion layers," *J. Power Sources*, vol. 154, no. 1, pp. 95–105, 2006.
- [14] S. Basu, C.-Y. Wang, and K. S. Chen, "Phase change in a polymer electrolyte fuel cell," *J. Electrochem. Soc.*, vol. 156, no. 6, pp. B748, 2009.
- [15] B. Straubhaar, J. L. Pauchet, and M. Prat, "Pore network modelling of condensation in gas diffusion layers of proton exchange membrane fuel cells," *Int. J. Heat Mass Transfer*, vol. 102, pp. 891–901, 2016.
- [16] B. Straubhaar, J. Pauchet, and M. Prat, "Water transport in gas diffusion layer of a polymer electrolyte fuel cell in the presence of a temperature gradient. Phase change effect," *Int. J. Hydrogen Energy*, vol. 40, no. 35, pp. 11668–11675, 2015. DOI: [10.1016/j.ijhydene.2015.04.027](https://doi.org/10.1016/j.ijhydene.2015.04.027).
- [17] L. Chen, H.-B. Luan, and W.-Q. Tao, "Liquid water dynamic behaviors in the GDL and GC of PEMFCS using lattice Boltzmann method," *Front. Heat Mass Transfer*, vol. 1, no. 2, pp. 023002, 2010. DOI: [10.5098/hmt.v1.2.3002](https://doi.org/10.5098/hmt.v1.2.3002).
- [18] W.-Z. Fang, L. Chen, Q.-J. Kang, and W.-Q. Tao, "Lattice Boltzmann modeling of pool boiling with large liquid-gas density ratio," *Int. J. Therm. Sci.*, vol. 114, pp. 172–183, 2017.
- [19] W.-Z. Fang, Y.-Q. Tang, C. Ban, Q. Kang, R. Qiao, and W.-Q. Tao, "Atomic layer deposition in porous electrodes: a pore-scale modeling study," *Chem. Eng. J.*, vol. 378, pp. 122099, 2019. DOI: [10.1016/j.cej.2019.122099](https://doi.org/10.1016/j.cej.2019.122099).
- [20] A. Xu, W. Shyy, and T. Zhao, "Lattice Boltzmann modeling of transport phenomena in fuel cells and flow batteries," *Acta Mech. Sin.*, vol. 33, no. 3, pp. 555–574, 2017.
- [21] P. Zhou and C. Wu, "Liquid water transport mechanism in the gas diffusion layer," *J. Power Sources*, vol. 195, no. 5, pp. 1408–1415, 2010.
- [22] G. R. Molaeimanesh and M. H. Akbari, "A pore-scale model for the cathode electrode of a proton exchange membrane fuel cell by lattice Boltzmann method," *Korean J. Chem. Eng.*, vol. 32, no. 3, pp. 397–405, 2015.
- [23] G. Molaeimanesh and M. Akbari, "A three-dimensional pore-scale model of the cathode electrode in polymer-electrolyte membrane fuel cell by lattice Boltzmann method," *J. Power Sources*, vol. 258, pp. 89–97, 2014.
- [24] X. Shan and H. Chen, "Lattice Boltzmann model for simulating flows with multiple phases and components," *Phys. Rev. E Stat. Phys.*, vol. 47, no. 3, pp. 1815–1819, 1993. DOI: [10.1103/physreve.47.1815](https://doi.org/10.1103/physreve.47.1815).
- [25] Q. Kang, D. Zhang, and S. Chen, "Displacement of a two-dimensional immiscible droplet in a channel," *Phys. Fluids*, vol. 14, no. 9, pp. 3203–3214, 2002.
- [26] Q. Li, K. Luo, and X. Li, "Lattice Boltzmann modeling of multiphase flows at large density ratio with an improved pseudopotential model," *Phys. Rev. E*, vol. 87, no. 5, pp. 053301, 2013. DOI: [10.1103/PhysRevE.87.053301](https://doi.org/10.1103/PhysRevE.87.053301).
- [27] W.-Z. Fang, Y.-Q. Tang, C. Yang, and W.-Q. Tao, "Numerical simulations of the liquid-vapor phase change dynamic processes in a flat micro heat pipe," *Int. J. Heat Mass Transfer*, vol. 147, pp. 119022, 2020. DOI: [10.1016/j.ijheatmasstransfer.2019.119022](https://doi.org/10.1016/j.ijheatmasstransfer.2019.119022).
- [28] S. Ponce Dawson, S. Chen, and G. D. Doolen, "Lattice Boltzmann computations for reaction-diffusion equations," *J. Chem. Phys.*, vol. 98, no. 2, pp. 1514–1523, 1993.

- [29] M. H. Bouzidi, M. Firdaouss, and P. Lallemand, "Momentum transfer of a Boltzmann-lattice fluid with boundaries," *Phys. Fluids*, vol. 13, no. 11, pp. 3452–3459, 2001.
- [30] S. D. Walsh and M. O. Saar, "Interpolated lattice Boltzmann boundary conditions for surface reaction kinetics," *Phys. Rev. E*, vol. 82, no. 6, pp. 066703, 2010. DOI: [10.1103/PhysRevE.82.066703](https://doi.org/10.1103/PhysRevE.82.066703).
- [31] M. Kamali, S. Sundaresan, H. van den Akker, and J. Gillissen, "A multi-component two-phase lattice Boltzmann method applied to a 1-D Fischer-Tropsch reactor," *Chem. Eng. J.*, vol. 207–208, pp. 587–595, 2012. vol
- [32] W.-Z. Fang, H. Zhang, L. Chen, and W.-Q. Tao, "Numerical predictions of thermal conductivities for the silica aerogel and its composites," *Appl. Therm. Eng.*, vol. 115, pp. 1277–1286, 2017.
- [33] J. Zhang, "Lattice Boltzmann method for microfluidics: models and applications," *Microfluid Nanofluid*, vol. 10, no. 1, pp. 1–28, 2011.
- [34] S. Huo, K. Jiao, and J. W. Park, "On the water transport behavior and phase transition mechanisms in cold start operation of PEM fuel cell," *Appl. Energy*, vol. 233–234, pp. 776–788, 2019. vol
- [35] Q. Kang, P. C. Lichtner, and D. Zhang, "An improved lattice Boltzmann model for multicomponent reactive transport in porous media at the pore scale," *Water Resour. Res.*, vol. 43, no. 12, pp. W12S14, 2007. DOI: [10.1029/2006WR005551](https://doi.org/10.1029/2006WR005551).
- [36] L. Chen, Q. Kang, B. A. Robinson, Y.-L. He, and W.-Q. Tao, "Pore-scale modeling of multiphase reactive transport with phase transitions and dissolution-precipitation processes in closed systems," *Phys. Rev. E*, vol. 87, no. 4, pp. 043306, 2013. DOI: [10.1103/PhysRevE.87.043306](https://doi.org/10.1103/PhysRevE.87.043306).
- [37] P. Yuan and L. Schaefer, "Equations of state in a lattice Boltzmann model," *Phys. Fluids*, vol. 18, no. 4, pp. 042101, 2006. DOI: [10.1063/1.2187070](https://doi.org/10.1063/1.2187070).